



Publication Year	2016
Acceptance in OA@INAF	2020-05-08T14:36:43Z
Title	High Mass High H I Mass, H I-rich Galaxies at $z < 0$: Observations
Authors	Hallenbeck, Gregory; Huang, Shan; Spekkens, Kristine; Haynes, Martha P.; Giovanelli, Riccardo; et al.
DOI	10.3847/1538-3881/152/6/225
Handle	http://hdl.handle.net/20.500.12386/24654
Journal	THE ASTRONOMICAL JOURNAL
Number	152



HIGHMASS—HIGH H I MASS, H I-RICH GALAXIES AT $Z \sim 0$: COMBINED H I AND H₂ OBSERVATIONS

GREGORY HALLENBECK¹, SHAN HUANG², KRISTINE SPEKKENS³, MARTHA P. HAYNES⁴, RICCARDO GIOVANELLI⁴,
ELIZABETH A. K. ADAMS⁵, JARLE BRINCHMANN⁶, JOHN CARPENTER⁷, JAYARAM CHENGALUR⁸, LESLIE K. HUNT⁹,
KAREN L. MASTERS^{10,11}, AND AMÉLIE SAINTONGE¹²

¹ Union College, Department of Physics & Astronomy, Schenectady, NY, USA; hallenbg@union.edu

² CCPP, New York University, 4 Washington Place, New York, NY 10003, USA; shan.huang@nyu.edu

³ Royal Military College of Canada, Department of Physics, P.O. Box 17000, Station Forces,
Kingston, ON K7K 7B4, Canada; Kristine.Spekkens@rmc.ca

⁴ Cornell Center for Astrophysics and Planetary Science (CCAPS), Space Sciences Building,
Cornell University, Ithaca, NY 14853, USA; haynes@astro.cornell.edu, riccardo@astro.cornell.edu

⁵ ASTRON, the Netherlands Institute for Radio Astronomy, Postbus 2, 7990 AA, Dwingeloo, The Netherlands; adams@astron.nl

⁶ Leiden Observatory, Leiden University, P.O. Box 9513, 2300 RA Leiden, The Netherlands; jarle@strw.leidenuniv.nl

⁷ California Institute of Technology, Department of Astronomy, MC 249-17, Pasadena, CA 91125, USA; jmc@astro.caltech.edu

⁸ National Centre for Radio Astrophysics, Tata Institute for Fundamental Research, Pune 411 007, India; chengalu@ncra.tifr.res.in

⁹ INAF-Osservatorio Astrofisico di Arcetri, Largo E. Fermi 5, I-50125, Firenze, Italy; hunt@arcetri.inaf.it

¹⁰ Institute of Cosmology and Gravitation, Dennis Sciama Building, Burnaby Road, Portsmouth PO1 3FX, UK; Karen.Masters@port.ac.uk

¹¹ South East Physics Network, Portsmouth, UK; <http://www.sepnet.ac.uk>

¹² University College London, Department of Physics & Astronomy, Kathleen Lonsdale Building,
Gower Place, London, WC1E 6BT, UK; a.saintonge@ucl.ac.uk

Received 2016 June 30; revised 2016 September 18; accepted 2016 September 27; published 2016 December 7

ABSTRACT

We present resolved H I and CO observations of three galaxies from the HighMass sample, a sample of H I-massive ($M_{\text{HI}} > 10^{10} M_{\odot}$), gas-rich (M_{HI} in the top 5% for their M_{*}) galaxies identified in the ALFALFA survey. Despite their high gas fractions, these are not low-surface-brightness galaxies and have typical specific star formation rates (SFR/M_{*}) for their stellar masses. The three galaxies have normal SFRs for their H₂ masses, but unusually short star formation efficiency scale lengths, indicating that the star formation bottleneck in these galaxies is in the conversion of H I to H₂, not in converting H₂ to stars. In addition, their dark matter spin parameters (λ) are above average, but not exceptionally high, suggesting that their star formation has been suppressed over cosmic time but is now becoming active, in agreement with prior H α observations.

Key words: galaxies: evolution – galaxies: individual (UGC 6168, UGC 7899, NGC 5230) – galaxies: spiral – radio lines: galaxies

1. INTRODUCTION

Star-forming galaxies in the local universe follow a tight correlation between specific star formation rate ($\text{SSFR} \equiv \text{SFR}/M_{*}$) and stellar mass known as the star-forming main sequence: as stellar mass increases, SSFR slowly decreases (e.g., Brinchmann et al. 2004; Salim et al. 2007; Schiminovich et al. 2007). This main sequence has been observed out to high stellar masses ($M_{*} > 10^{10} M_{\odot}$) in the optically selected GASS survey (the GALEX Arcibo SDSS survey; Catinella et al. 2010; Schiminovich et al. 2010). However, optically selected samples are inherently biased toward galaxies with higher surface brightnesses. In comparison to optical samples, samples selected by H I are bluer and have higher gas fractions ($\text{GF} \equiv M_{\text{HI}}/M_{*}$), lower star formation efficiencies ($\text{SFE} \equiv \text{SFR}/M_{\text{HI}}$), and lower surface brightnesses than optically selected samples (e.g., Huang et al. 2012b). Given the strong differences between optically and H I-selected samples, it is not immediately clear whether galaxies with high H I masses also follow the star formation main sequence.

Consider the “H I Monsters” sample of Lee et al. (2014) and the Bluedisks sample of Wang et al. (2013), which were selected on the basis of H I mass, either directly from the ALFALFA survey (in the case of the H I Monsters) or as inferred from optical colors (Bluedisks), with each sample yielding H I masses of $M_{\text{HI}} > 10^{10.5} M_{\odot}$ and $10^{8.3} M_{\odot} < M_{\text{HI}} < 10^{10.4} M_{\odot}$, respectively. The H I Monsters

have high H I masses and correspondingly high $M_{*} \sim 10^{11} M_{\odot}$ and $M_{\text{H}_2} \sim 10^{10} M_{\odot}$. They also have quite high SFRs, and their SSFRs lie on the star-forming main sequence. The Bluedisks galaxies’ H I radii follow scaling relations derived for lower- M_{HI} galaxies. Additionally, their H I disks do not appear disturbed, suggesting that they had not recently acquired gas from a merger. It appears that selecting on the basis of H I mass alone yields samples that are similar to lower-mass spiral galaxies, but “scaled up” to higher total mass. As gas fraction decreases with increasing stellar mass, these samples consist of H I-massive but not particularly gas-rich galaxies. Instead, the typical gas fractions of both samples are in the range $0.1 < \text{GF} < 1.0$.

Many galaxies that are both H I-massive ($M_{\text{HI}} > 10^{10} M_{\odot}$) and gas-rich ($\text{GF} \gtrsim 1$) deviate from the star-forming main sequence. Some are giant, low-surface-brightness galaxies (GLSBs) like Malin 1 ($M_{\text{HI}} = 10^{10.8} M_{\odot}$, $\text{GF} \approx 0.9$; Bothun et al. 1987; Lelli et al. 2010). GLSBs are also seen to also exhibit low surface densities of H I. Lemonias et al. (2014) examined an optically selected sample of GASS galaxies with $M_{\text{HI}} > 10^{10} M_{\odot}$ and high gas fractions. As a whole, the sample has suppressed star formation, lying in the same region of M_{*} – SSFR space as GLSBs. Karl G. Jansky Very Large Array (VLA) observations of the sample show that these galaxies have extended, low average deprojected H I surface density (Σ_{HI}), as well as low deprojected SFR surface density (Σ_{SFR}).

From the 40% sky area data release of the ALFALFA survey ($\alpha.40$; Haynes et al. 2011), we have identified the HIghMass sample, first presented in Huang et al. (2012b). Like the sample of Lemonias et al. (2014), the HIghMass galaxies are selected to have both a high H I mass ($M_{\text{HI}} > 10^{10} M_{\odot}$) and unusually high gas fractions for their stellar masses (gas fraction is 1σ above average). This yields a sample with $\text{GF} \gtrsim 0.4$; half have $M_{\text{HI}} > M_{*}$. Despite these high gas fractions, unlike the optically selected sample of Lemonias et al. (2014), the HIghMass galaxies do not have suppressed star formation: they fall along the SSFR – M_{*} star-forming main sequence.

The only sample with properties similar to HIghMass is H I GHz (Catinella & Cortese 2015). The H I GHz galaxies are similarly massive ($M_{\text{HI}} > 10^{10} M_{\odot}$) and gas-rich ($0.1 < \text{GF} < 2$), while also lying on or above the star-forming main sequence. The galaxies of the H I GHz sample lie at $0.17 \leq z \leq 0.25$ and are massive galaxies that are still assembling their disks. The HIghMass galaxies are at a redshift of $z < 0.06$, suggesting that the HIghMass galaxies are the low-redshift analogs of the H I GHz sample. But how can massive gaseous reservoirs like those observed in the HIghMass galaxies survive to $z = 0$ in galaxies whose star formation is not suppressed? Our hypotheses broadly fall into two categories. First, the galaxies have unusually high dark matter halo spin parameters, suppressing time-averaged star formation. Second, their cold gas has been recently acquired.

The dark matter spin parameter is a dimensionless way to quantify the angular momentum of a dark matter halo, $\lambda \equiv J |E|^{1/2} G^{-1} M^{-5/2}$. Theoretically, high spin parameters are associated with bluer colors, lower optical surface brightness, and higher gas fractions (e.g., Jimenez et al. 1998; Mo et al. 1998; Boissier & Prantzos 2000; Macciò et al. 2007). Unfortunately, λ is ultimately a parameter that is not directly observable. Despite this, several works have attempted to infer it for populations of galaxies based on optical (Hernandez et al. 2007; Cervantes-Sodi & Hernández 2009) and a combination of optical and H I properties (Huang et al. 2012b), with results agreeing with theory. Huang et al. (2012b) found that the ALFALFA population as a whole has elevated values of λ compared with a Sloan Digital Sky Survey (SDSS) selected sample (Hernandez et al. 2007). Huang et al. (2014) further suggest that the HIghMass galaxies have, on average, even higher values of λ than the overall ALFALFA sample.

Recent gas can come from a “galactic fountain” effect, where supernovae have ionized and ejected gas (Fraternali & Binney 2006, 2008; Oppenheimer et al. 2010). While outside of the galactic disk, the gas is unable to form stars. Over time, the gas can cool, recombine, and return to the disk. Studies of NGC 891 and NGC 2403 (Fraternali & Binney 2008) at a distance of < 10 Mpc have inferred reaccretion rates as high as $1\text{--}3 M_{\odot} \text{ yr}^{-1}$, similar to their SFRs. Simulations by Marinacci et al. (2010) find that, in most cases, this extraplanar gas is unlikely to be of high enough column density to be observed directly, but can contribute to a galaxy’s global profile—that is, there can exist gas that is unable to contribute to star formation but will contribute to the H I mass observed by ALFALFA. Such gas shares a common specific angular momentum with the existing gaseous disk, but can cause inflows (Fraternali et al. 2001). Alternatively, recently acquired gas may originate in the intergalactic medium, having been unassociated with any galaxy until now. Such gas has angular momentum that is

uncorrelated with the galaxy’s disk, leading to warps as well as flows (Fraternali & Binney 2008).

Previous work by Hallenbeck et al. (2014) examined in detail two of the HIghMass galaxies using ~ 3 kpc resolution VLA observations. The two galaxies have quite similar optical photometric and unresolved H I spectral properties: $M_{*} > 10^{10} M_{\odot}$, $M_{\text{HI}} > 10^{10.3}$, specifically with $M_{\text{HI}} > M_{*}$. However, upon resolving the H I, we see that the two galaxies are drastically different. One (UGC 12506) is a low-surface-brightness (LSB) galaxy with a very high dark matter halo spin parameter ($\lambda = 0.15$), low surface density, extended H I (typically $1\text{--}5 M_{\odot} \text{ pc}^{-2}$ at radii from 10–40 kpc), and low star formation surface densities. The other (UGC 9037) has an elevated high spin parameter ($\lambda = 0.07$), but has both high central H I surface density ($> 10 M_{\odot} \text{ pc}^{-2}$ at radii less than 10 kpc) and centrally peaked star formation. In addition, UGC 9037 has what appear to be high-velocity inflows at all radii, with a peak noncircular $v = 0.09 v_{\text{rotation}}$, suggesting that the galaxy is undergoing a transition to a more intense star-forming phase.

This paper is the second in a series, building on the results of Hallenbeck et al. (2014). We present observations of the ^{12}CO (1–0) line (as a proxy for H_2), observed using CARMA (the Combined Array for Research in Millimeter-wavelength Astronomy) for three galaxies, UGC 6168, UGC 7899, and NGC 5230 (which is also UGC 8573). These three galaxies were specifically selected for study because they had the highest predicted CO column density using the scaling relations derived by Saintonge et al. (2011a). These new observations are combined with the $\text{H}\alpha$ studies of Huang et al. (2014) to examine disk stability and the SFE of the H I and H_2 phases and to determine whether the star formation bottleneck is in the conversion of H I to H_2 , or H_2 to stars. In addition, in order to test the recent accretion hypothesis, we are studying the resolved gas velocity fields to search for gas inflows and warps. Finally, we directly derive values of λ for each galaxy.

Much of our data reduction mirrors that in the previous work of Hallenbeck et al. (2014). We summarize and discuss differences from that previous work in Section 2. Results for each individual galaxy are presented in Section 3. We discuss possible evolutionary histories for each galaxy, as well as the HIghMass sample in general, in Section 4. Our conclusions are summarized in Section 5.

2. OBSERVATIONS AND DATA REDUCTION

In Table 1 we present the global gas, stellar, and star formation properties of the three HIghMass galaxies studied in this work, as well as the two galaxies studied by Hallenbeck et al. (2014). Except as described in the following sections, data reduction and analysis methods for gas are identical to those in Hallenbeck et al. (2014); methods for deriving stellar and star formation properties follow the methods of Huang et al. (2014). We provide a brief summary of those methods as follows:

1. Total H I masses, recession velocities, and distances are taken from the $\alpha.40$ catalog (Haynes et al. 2011), which assumes $H_0 = 70 \text{ km s}^{-1} \text{ Mpc}^{-1}$.
2. H I observations were performed at the VLA and the Giant Metrewave Radio Telescope (GMRT); data reduction uses a combination of standard CASA and GIPSY packages. These methods recover the total H I flux of our galaxies and produce line profiles that agree with the single-dish $\alpha.40$ catalog.

Table 1
Sample Optical and Radio Properties

Galaxy	d (Mpc)	$\log M_{\text{HI}}$ (M_{\odot})	$\log M_{\text{H}_2}$ (M_{\odot})	R_{25} (kpc)	$\log M_{*}$ (SED) (M_{\odot})	$\log M_{*}$ (IRAC) (M_{\odot})	$\log \text{SFR}$ ($M_{\odot} \text{ yr}^{-1}$)
(1)	(2)	(3)	(4)	(5)	(6)	(7)	(8)
UGC 6168	120	10.35	8.96	23.8	10.37	10.59	0.57
UGC 7899	128	10.42	9.68	36.8	10.49	10.93	1.20
NGC 5230	101	10.53	10.02	36.3	10.89	11.22	0.96
UGC 9037	88	10.33	...	23.0	10.09	...	0.56
UGC 12506	98	10.53	...	40.0	10.46	...	0.40 ^a

Note. Optical and radio properties of the HighMass galaxies in this work and in Hallenbeck et al. (2014). Column (1): galaxy identifier. Column (2): Hubble flow distance of galaxy, from Haynes et al. (2011). Column (3): H I mass, from Haynes et al. (2011). Column (4): inferred H₂ mass from CARMA observations of ¹²CO ($J = 1-0$) line. Column (5): radius of the 25 mag arcsec⁻² isophote in r band. Column (6): stellar mass, derived from fitting SEDs to SDSS magnitudes, from Huang et al. (2012b). Column (7): stellar mass, derived from *Spitzer* observations, and the mass-to-light ratios of Querejeta et al. (2014). Column (8): H α -derived SFRs, from Huang et al. (2014).

^a The SFR of UGC 12506 is an exception and is derived from SED-fitting its SDSS magnitudes.

- Rotation curves are derived by fitting tilted rings to the observed moment 1 velocity fields using the GIPSY task ROTCUR, with radii spaced every half beam width. Noncircular velocities are then reexamined and confirmed using the DiskFit package (Spekkens & Sellwood 2007; Sellwood & Sánchez 2010; Kuzio de Naray et al. 2012).
- SFRs and surface densities are calculated from H α imaging taken at Kitt Peak National Observatory (KPNO). We take the resulting profiles directly from Huang et al. (2014).
- Dark matter properties are determined by fitting to the observed rotation curves using the GIPSY task ROTMAS. We model each galaxy as having thin gas (H I, H₂, and He) and stellar components along with dark matter.
- A modified dark matter halo spin parameter λ' is calculated directly from the resolved gas properties and the dark matter halo fit (Equations (4), (5), and (6) from Hallenbeck et al. 2014):

$$\lambda' = \frac{J_{\text{HI}} |E|^{1/2}}{GM^{5/2}} = \frac{1}{2} \frac{\sum_i \frac{M_{\text{HI},i}}{M_{\text{HI}}} V_i r_i \cdot V_C^2}{GM^{1/2}}, \quad (1)$$

where $M_{\text{HI},i}$, V_i , and r_i are the H I mass, velocity, and galactocentric radius of each tilted ring, respectively, V_C is the maximum circular velocity of a fit pseudo-isothermal halo, and M is the mass of the dark matter halo. M is obtained via abundance matching of both the combined stellar and H I masses (Papastergis et al. 2012).

2.1. CO Observations and Inferred H₂ Properties

The three HighMass galaxies were observed using CARMA in its compact E configuration. The CARMA visibilities for the three galaxies are exported from the native MIRIAD format into CASA before following the same data reduction techniques as were performed for the H I observations. The VLA has a primary beam FWHM of $\sim 30'$ when observing the 21 cm H I line. However, at 115 GHz, the CARMA primary beam scale is $\sim 1'$, similar to the sizes of our galaxies (major axes $\sim 1'$). We image out to the 20% response contour and correct the fluxes accordingly.

Single-dish ¹²CO(1–0) observations of 18 HighMass galaxies were performed with the 30 m IRAM telescope, including UGC 6168, UGC 7899, and NGC 5230. For all three

galaxies, we produced spectra from the CARMA data cubes corresponding to the $22''$ field of view of the 30 m IRAM dish. The fluxes derived from these spectra agree with the fluxes derived from the single-dish observations (S. Huang et al. 2017, in preparation).

We must assume a conversion factor between the observed CO luminosity L'_{CO} (in units of $\text{K km s}^{-1} \text{ pc}^2$) and the total H₂ mass, known as α_{CO} . The conversion factor is known to vary with metallicity (e.g., Wilson 1995; Arimoto et al. 1996; Bolatto et al. 2013; Sandstrom et al. 2013). However, even though the HighMass galaxies are gas dominated, they all have $M_{*} \gtrsim 10^{10} M_{\odot}$, and thus we expect them to have metallicities similar to the Milky Way. We follow Saintonge et al. (2011a) and use a Milky Way value for α_{CO} averaged over several recent measurements (Strong & Mattox 1996; Dame et al. 2001; Blitz et al. 2007, Draine et al. 2007; Heyer et al. 2009; Abdo et al. 2010), $\alpha_{\text{CO}} = 3.2 M_{\odot} (\text{K km s}^{-1} \text{ pc}^2)^{-1}$. Given the conversion factor, we then compute the total H₂ mass following Solomon et al. (1997):

$$M_{\text{H}_2} = L'_{\text{CO}} \alpha_{\text{CO}} = 3.25 \times 10^7 \alpha_{\text{CO}} S_{\text{CO}} \nu^{-2} d^2 \quad (2)$$

where S_{CO} is the total integrated CO flux in Jy km s^{-1} (which are our intensity map units), ν is the rest frequency of the line in GHz, which for ¹²CO(1–0) is 115.271 GHz, and d is the Hubble flow distance of the galaxy in Mpc.

Production of H₂ moment maps, fitting of rotation curves, and derivation of deprojected surface densities then follow the same method as for H I. However, in most cases, the CO is only partially resolved by CARMA, and so we must assume inclinations and position angles as derived by the H I rotation curves.

2.2. Stellar Masses

Hallenbeck et al. (2014) used a combination of two methods to calculate stellar masses. Global stellar masses were calculated based on fitting model spectral energy distributions to SDSS magnitudes (Salim et al. 2007; Huang et al. 2012a, 2012b). These were then used to constrain the less precise surface density profiles following the method of Bell et al. (2003).

Here, instead of relying on optical photometry, we use infrared $3.6 \mu\text{m}$ and $4.5 \mu\text{m}$ photometry taken with *Spitzer* IRAC (Fazio et al. 2004; Werner et al. 2004), which should

trace the old stellar population. We then convert to stellar masses following Equation (4) of Querejeta et al. (2014):

$$\log \Upsilon_{3.6} = -0.339([3.6] - [4.5]) - 0.336 \quad (3)$$

where $\Upsilon_{3.6}$ is the mass-to-light ratio of the $3.6 \mu\text{m}$ band and $[3.6]-[4.5]$ is the color from the $3.6 \mu\text{m}$ and $4.5 \mu\text{m}$ bands. For UGC 6168, UGC 7899, and NGC 5230, the IRAC stellar masses are larger by a factor of 2–3 compared with the SED fit masses. It is possible that this method is overestimating our stellar masses because the IRAC bands may have hot dust contamination as a result of dust heating by active star formation.

2.3. Stability Criteria

When calculating the stability of the disk via the Toomre Q parameter, the work of Hallenbeck et al. (2014) neglected the contribution from stars. For both galaxies, the stellar mass was quite centrally concentrated by comparison with the H I. In addition, $M_* < M_{\text{H I}}$. As a consequence, simple two-phase models of the galaxy disk, such as those by Wang & Silk (1994) and Rafikov (2001), predicted essentially no change in Q at all radii.

However, the inclusion of H_2 requires serious consideration. As H_2 is much cooler and has a higher per-particle mass than H I, its turbulent velocity is lower. As a consequence, for the same gas surface density, H_2 is less stable. Therefore, in this paper we also consider the method of Romeo & Wiegert (2011) and Romeo & Falstad (2013). Their Q_N accounts for an arbitrary number of phases. It is defined as (see Equation (19) of Romeo & Falstad 2013)

$$\frac{1}{Q_N} = \sum_i \frac{\pi G \Sigma_i W_i}{\sigma_i \kappa(r) T_i} \quad (4)$$

The first factor is the Toomre Q parameter (Toomre 1964) for each particular phase, consisting of Newton’s gravitational constant G , the surface density of the phase Σ_i , the velocity dispersion of the phase σ_i , and the epicyclic frequency $\kappa(r)$ calculated from the rotation curve. W_i and T_i are dimensionless parameters of order unity; these account for the overall stability being dominated by the most stable phase and the effect of the finite thickness of the disk, respectively (see Equations (16) and (18) from Romeo & Falstad 2013). Following Romeo & Falstad (2013), we use $\sigma_{\text{H}_2} \approx 6 \text{ km s}^{-1}$ (Wilson et al. 2011) and $\sigma_{\text{H I}} \approx 11 \text{ km s}^{-1}$ (Leroy et al. 2008).

In the rest of this work, when we refer to “Toomre Q ,” we mean that we are treating all of the gas (H I, H_2 , and He) as a single phase with $\sigma_{\text{gas}} = 11 \text{ km s}^{-1}$, with He included as a factor of 1.33 correction to the mass. This will accurately model the H I, but will overestimate the stability of the H_2 from an artificially high σ_{H_2} . “ Q_N ” refers to the multiphase stability criterion of Romeo & Falstad (2013), which properly accounts for the cold H_2 .

3. RESULTS

3.1. Overview of UGC 6168

In the top panels of Figure 1, we present the integrated flux maps for our H I (left) and CO (right) synthesis observations of UGC 6168. The contours begin at and are spaced every $5 M_\odot \text{pc}^{-2}$ of H I or inferred H_2 mass, as projected onto the sky.

These contours are then overlaid on SDSS r -band images. The top left panel shows the H I integrated flux map. Like the other two galaxies in this work, UGC 6168 is a spiral galaxy. Huang et al. (2014) note that the color gradient in UGC 6168 reverses, that is, as radius increases, the average color of the galaxy first becomes bluer and then redder in the outer disk. Color inversions may be related to declining star formation, dust-obscured central star formation, and outward migration of stars. This color gradient reversal is also a feature of UGC 7899 and NGC 5230.

The H I is extended beyond the optical radius, as is typical for a gas-rich galaxy. In addition, the H I within 5 kpc of the galaxy’s center is clearly depleted, leaving a hole. This is unsurprising: the galaxies discussed in this work were specifically observed because they had the highest expected H_2 masses out of the HIghMass sample. They are thus likely to be some of the most efficient at transforming gas into new stars. The top right panel shows the H_2 distribution, as inferred from the CO emission. It very neatly fills in the hole left by the H I.

The bottom panels of Figure 1 show the velocity fields of the H I (left) and CO (right). Isovelocity contours are spaced every 20 km s^{-1} . The CO emission is not sufficiently resolved by our $10''$ clean beam, and so no rotation curve can be fit. We nonetheless fit an average position angle, and the best fit for each phase is overlaid. We note that the rotational axis of each phase is clearly different, which is indicative of noncircular flows.

Figure 2 presents the rotation curve of UGC 6168 derived from a tilted ring fit. The top left panel shows the rotation velocity as a function of radius. This rotation curve is derived with constant PA = $296^\circ.1$ north of west and $i = 59^\circ.2$. UGC 6168’s rotation increases slowly to $\sim 200 \text{ km s}^{-1}$ over the 35 kpc for which we can trace the gas, and appears to still be rising. Our ROTCUR model of the galaxy includes strong noncircular motions (top right panel) within 25 kpc of the galaxy’s center. These noncircular velocities reach 40% of the galaxy’s rotation speed, significantly higher than the 9% observed in the “marginally unstable” UGC 9037 by Hallenbeck et al. (2014). It must be noted, however, that the signs of the noncircular velocities are degenerate with galaxy geometry, and these could be associated with either inward or outward flows. ROTCUR underestimates the uncertainties of the noncircular velocities. Fitting the galaxy’s rotation curve with DiskFit—which more accurately estimates the uncertainties—indicates that models of radial or bar-like flows are of 1σ – 2σ significance.

Figure 3 shows the deprojected surface density profiles of both the H I (closed circles) and H_2 (open circles). The solid black line is the total gas density. The stars depict the star formation surface density (from Huang et al. 2014, Figure 15). In the inner disk, the total gas density remains relatively constant at $\sim 10 M_\odot \text{pc}^{-2}$ (cyan triple-dot-dashed line), a surface density beyond which there is rarely H I at solar metallicities (e.g., Bigiel et al. 2008); at solar abundance, gas above this threshold tends to be entirely molecular. This is the “saturation line” referred to in this and subsequent figures. The upper red dotted line indicates a gas surface density corresponding to an unstable ($Q < 1$; upper line) thin gas disk. Generally, widespread disk instability is not observed in the local universe; any time gas surface densities exceed this value, it is likely a failure of the single-phase thin gas disk model (for discussion of a more realistic Q_N model for all three galaxies, see Section 3.4).

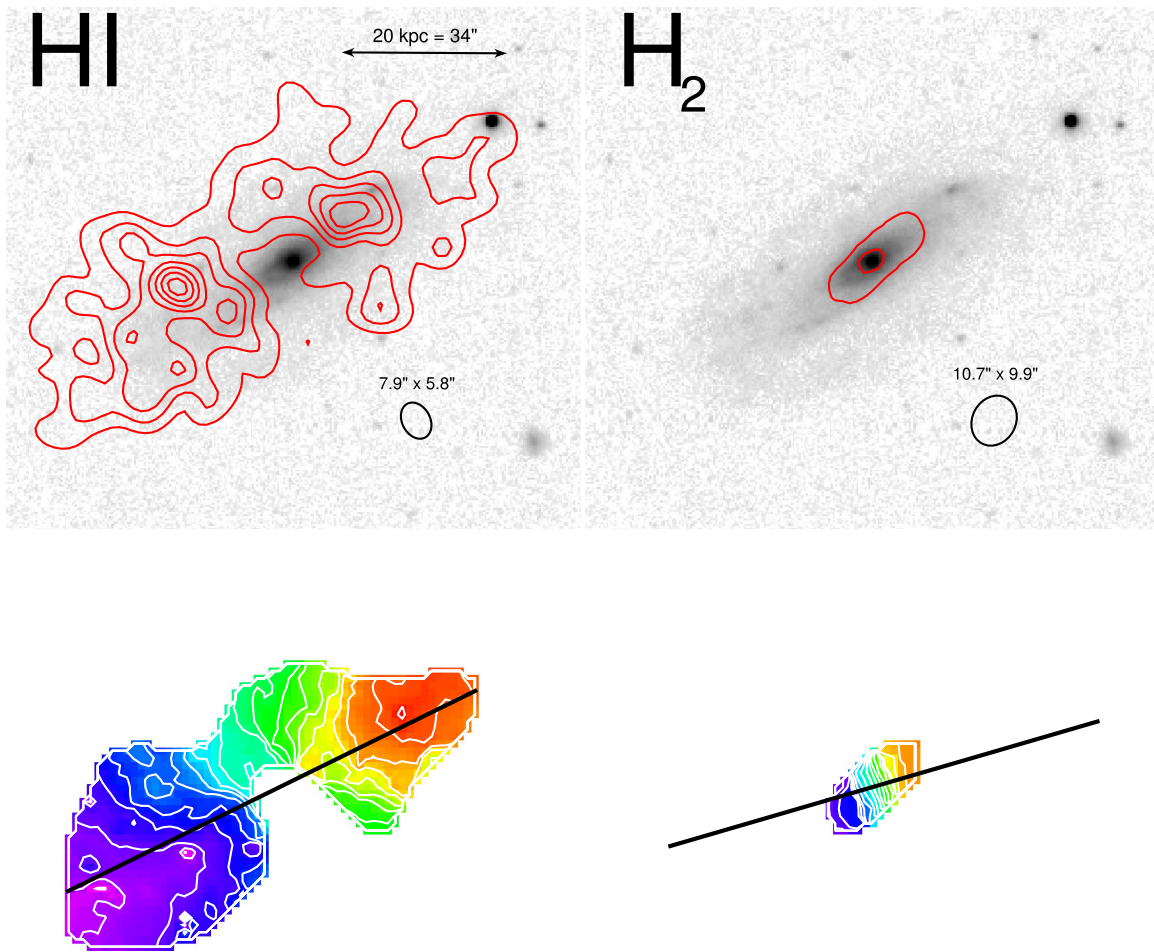


Figure 1. Top: H I (left) and CO (right) integrated flux maps of UGC 6168. Contours begin at and are spaced every $5 M_{\odot} \text{pc}^{-2}$ of either H I or inferred H_2 . Both contours are overlaid on an inverted SDSS r -band image. Bottom: H I (left) and CO (right) velocity fields, with isovelocity contours spaced every 20 km s^{-1} . The H I is depleted in the center and appears in the shape of a ring. While the CO is just barely resolved, the major axes of rotation for the H I and CO are different (black lines), which suggests the presence of noncircular flows in the galaxy.

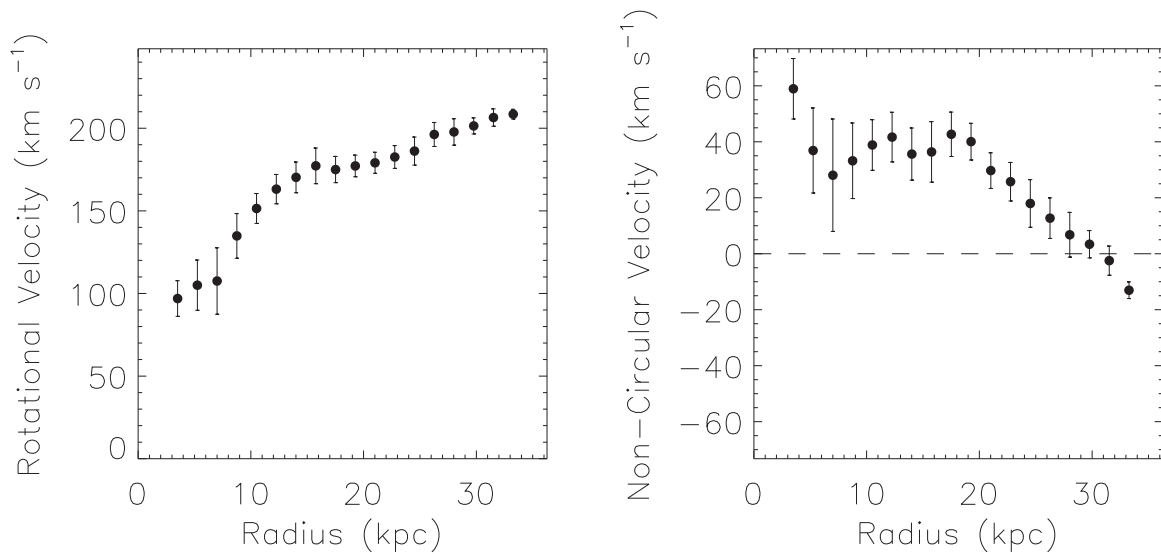


Figure 2. Rotation curve of UGC 6168 derived by fitting a tilted ring model to the H I velocity field. The panels show rotation velocity (left) and radial noncircular velocity (right), either “expansion” or “contraction.” PA is fixed at $296^{\circ}.1$ north of west, and inclination is fixed at $i = 59^{\circ}.2$. The rotation of the H I rises slowly and appears to be still rising to velocities $>200 \text{ km s}^{-1}$ at the last point measured.

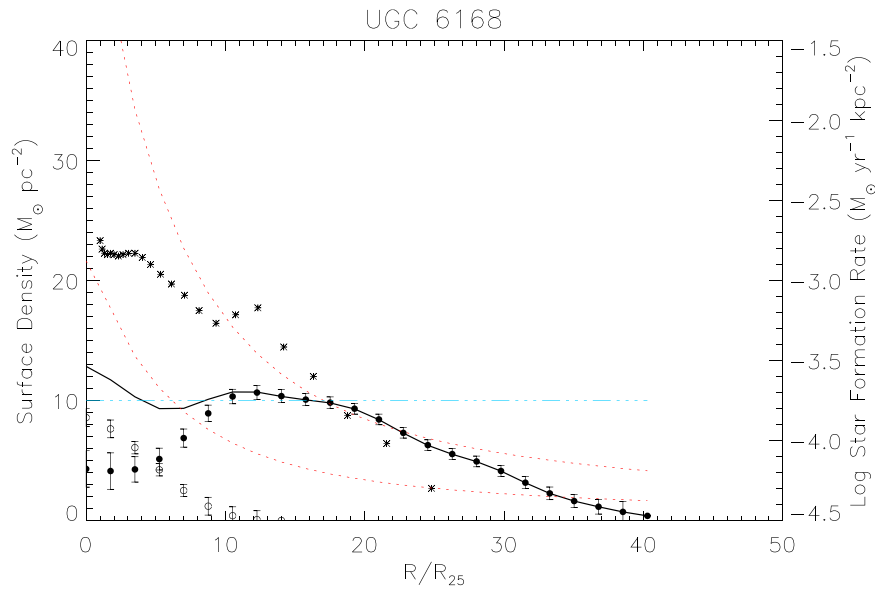


Figure 3. Surface density profile of the H I (filled circles) and H₂ (open circles), as inferred from CO emission, of UGC 6168. The solid line is the total gas surface density. Crosses are the H α -derived star formation surface density (from Huang et al. 2014, Figure 15). Red dotted lines indicate where the gas surface density is 0.4 times (lower) and equal to (upper) the density at which the gas would be unstable according to its Toomre Q parameter. The cyan triple-dot-dashed line is located at $10 M_{\odot} \text{pc}^{-2}$, where H I is observed to saturate in the local universe. At small galactocentric radii, there is little H I, but the total gas surface density remains constant. Between 10 and 30 kpc, the galaxy is marginally unstable, and it approaches instability near 20 kpc.

However, at surface densities corresponding to $Q \lesssim 2.5$ (lower red dotted line), star formation is observed to be enhanced (Kennicutt 1989; Martin & Kennicutt 2001; Leroy et al. 2008). We refer to $1 < Q < 2.5$ as the “marginally unstable” regime. For UGC 6168, the gas disk is predicted to be stable in the interior 7 kpc and at $r > 18$ kpc and is marginally unstable at intermediate radii. This marginal instability coincides with an SFR enhancement near 12–15 kpc. However, overall star formation is peaked at the center of the galaxy, where we predict the gas to be stable.

3.2. Overview of UGC 7899

Images, surface density contours, and velocity fields of UGC 7899 appear in Figure 4; the panels are identical to Figure 1. Like UGC 6168, UGC 7899 is an inclined spiral galaxy, with $i \sim 72^\circ$. It also exhibits a color reversal, where the galaxy exhibits redder colors at larger radii than at intermediate radii (Huang et al. 2014). A close inspection also reveals that the optical galaxy is not perfectly symmetric: it tapers, with the optical emission at the northern edge of the galaxy more extended than at the southern edge.

The H I and inferred H₂ contours begin at projected $5 M_{\odot} \text{pc}^{-2}$ and increase by $5 M_{\odot} \text{pc}^{-2}$ at each additional contour. The H I in the center of UGC 7899 is not depleted: there is no H I ring. Instead, its surface density becomes approximately constant. There are, however, high H₂ surface densities—much higher densities than are observed in either UGC 6168 or UGC 7899, reaching a projected column density of $\sim 50 M_{\odot} \text{pc}^{-2}$ (corresponding to roughly $25 M_{\odot} \text{pc}^{-2}$ when deprojected). The contours on the southern side of the galaxy suggest a slight warp in the H I disk at large radii.

The bottom panels show the velocity fields of the H I (left) and CO (right). The H I velocity field appears slightly asymmetric, suggesting a warp in the outermost part of the disk. Like UGC 6168, the CO is only marginally resolved at the scale of the CARMA beam, and no rotation curve can be fit.

Figure 5 presents the results of tilted ring fits to the UGC 7899’s H I velocity field (black circles). The best-fit constant PA and i are PA = $39^\circ.8$ north of west and $i = 71^\circ.1$. The rotation curve rises linearly to $\sim 180 \text{ km s}^{-1}$ and then changes to a shallower slope, reaching a maximum of $\sim 230 \text{ km s}^{-1}$. The fit becomes uncertain at large radii because of the north-south mismatch mentioned above: we find a declining rotation curve in the southern approaching half of the galaxy, but not in the northern receding half. DiskFit suggests that these observed noncircular flows are of marginal (1σ – 2σ) significance, and only in the outer regions. Because geometry and noncircular velocities are degenerate, we fit a second model to the map to capture the effect of the galaxy’s warp (red circles). This model holds fixed both the rotation curve and a radial flow of 0 km s^{-1} . Here we observe a relatively constant position angle, which changes abruptly by 4° at a galactocentric radius of 25 kpc.

Figure 6 presents deprojected surface densities of H I and H₂ as a function of radius. Also included are our $Q < 1$ and $Q < 2.5$ stability curves and a $\Sigma_{\text{H I}} = 10 M_{\odot} \text{pc}^{-2}$ saturation line. Unlike UGC 6168, there is no H I hole in the center of the galaxy. Instead, the H I saturates at $10 M_{\odot} \text{pc}^{-2}$, while Σ_{H_2} reaches nearly $30 M_{\odot} \text{pc}^{-2}$, 50% higher than either of the other two galaxies in this work. We predict that the disk is marginally unstable for $r < 30$ kpc, with the disk at or near instability for $r < 20$ kpc. This is in agreement with the observation that the most active star formation in UGC 7899 is centrally located.

3.3. Overview of NGC 5230 (UGC 8573)

Figure 7 presents the H I and CO moment maps of NGC 5230. NGC 5230 is a large spiral galaxy with a low inclination ($i \sim 20^\circ$). Its southern arm appears less tightly wound than the other two in the north. Like UGC 6168, there is a large central hole where the H I has essentially all been converted into H₂. However, the H I hole in NGC 5230 is larger, with a radius of 10–15 kpc, and has no H I down to our detection limits of

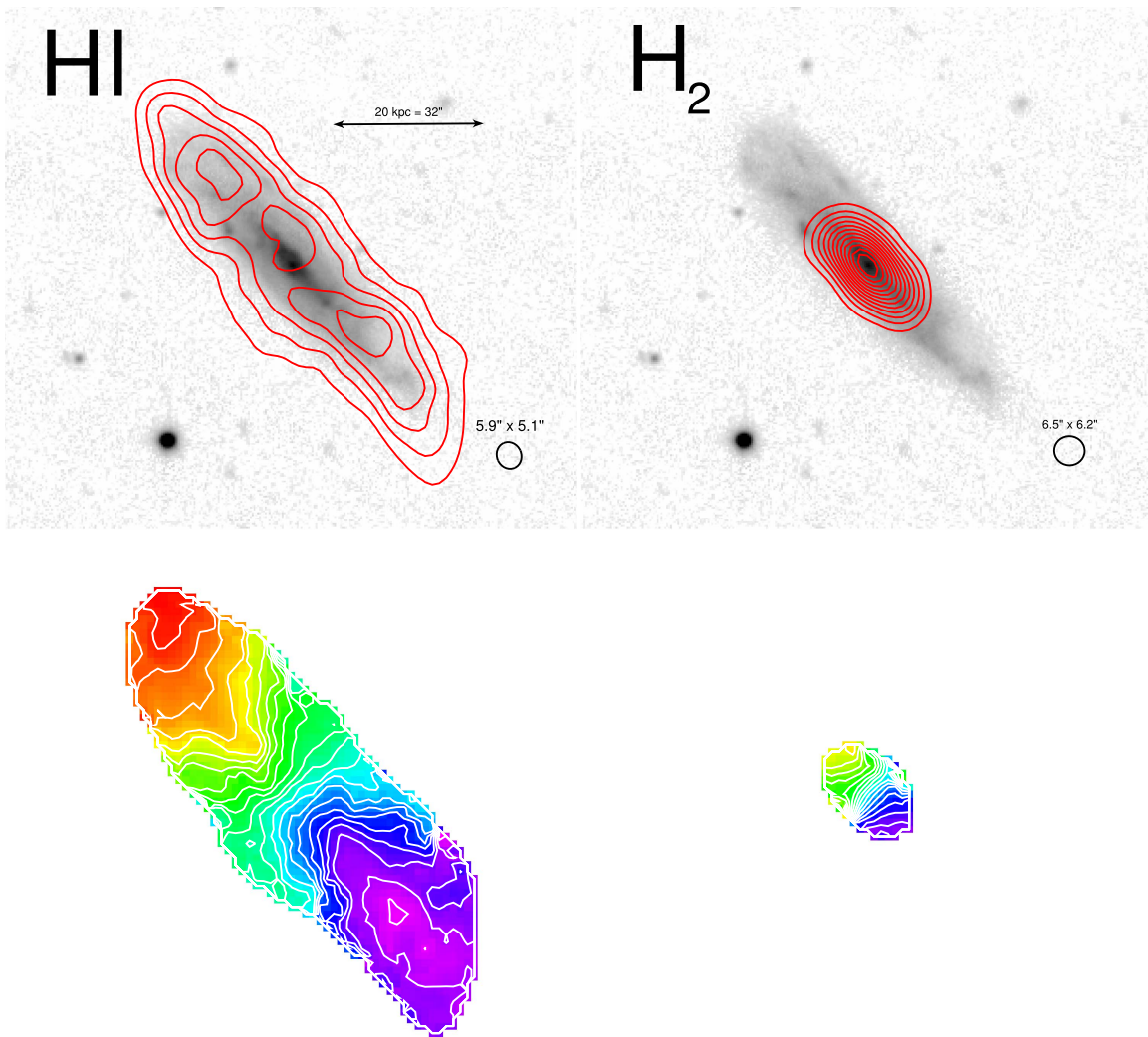


Figure 4. Integrated flux maps and velocity fields of UGC 7899. Panels are identical to Figure 1. The projected surface densities of CO in UGC 7899 are much higher than either UGC 6168 or NGC 5230, reaching $50 M_{\odot} \text{pc}^{-2}$ ($\sim 25 M_{\odot} \text{pc}^{-2}$ deprojected). The H I rotation shows some asymmetry: there are closed contours on the southern (approaching) half of the galaxy, indicative of a likely warp in the H I disk at large galactocentric radii, which is absent in the northern (receding) half of the galaxy.

$1.63 M_{\odot} \text{pc}^{-2}$. All three spiral arms show enhanced densities of H₂, out to CARMA’s half-power response radius (dashed line). We thus cannot know whether all of the CO has been mapped. Regardless, we have adequately mapped the CO emission of the inner $30''$ (~ 15 kpc).

Because of the low inclination of NGC 5230 ($i < 40^{\circ}$), fitting a rotation curve and deriving surface densities from H I velocity fields via tilted ring fits (Begeman 1989) is highly unreliable. We thus remove it from our later surface density, rotation curve, and dark matter fitting except as noted.

3.4. Multiphase Stability Parameter

Figure 8 presents the multiphase Q_N of Romeo & Falstad (2013) for both UGC 6168 (red triangles) and UGC 7899 (green squares). The radii have been normalized by r -band R_{25} , the radius at which the isophotes reach $25 \text{ mag arcsec}^{-2}$. The dashed line indicates a value of $Q_N = 1$. For values of $Q_N < 1$, the disk is unstable to perturbations, while for $Q_N > 1$, the disk is stable.

Both galaxies show similar trends: they are predicted to be stable beyond the optical disk ($R > R_{25}$) and are marginally unstable ($Q_N \lesssim 2.5$) in the region $0.5 < R/R_{25} < 1.0$. In the inner disk ($R < 0.5 R_{25}$), UGC 6168 becomes stable again, but the high surface densities of H₂ cause UGC 7899 to become unstable. Neither disk is predicted to be unstable to ring-like perturbations.

These results are not greatly different from the one-phase Toomre Q results discussed in the previous sections. The only significant change is that for UGC 6168, the multiphase model predicts a marginally unstable ($Q_N \lesssim 2.5$) disk at intermediate radii, while the single-phase model predicts a fully unstable disk.

3.5. H I Radii

For both typical spiral galaxies and more massive spiral galaxies, there exists a tight linear correlation between the total H I gas mass and the radius at which the deprojected surface density reaches $1 M_{\odot} \text{pc}^{-2}$ (Broeils & Rhee 1997; Wang et al. 2013, 2016). This relationship can be expressed as (from

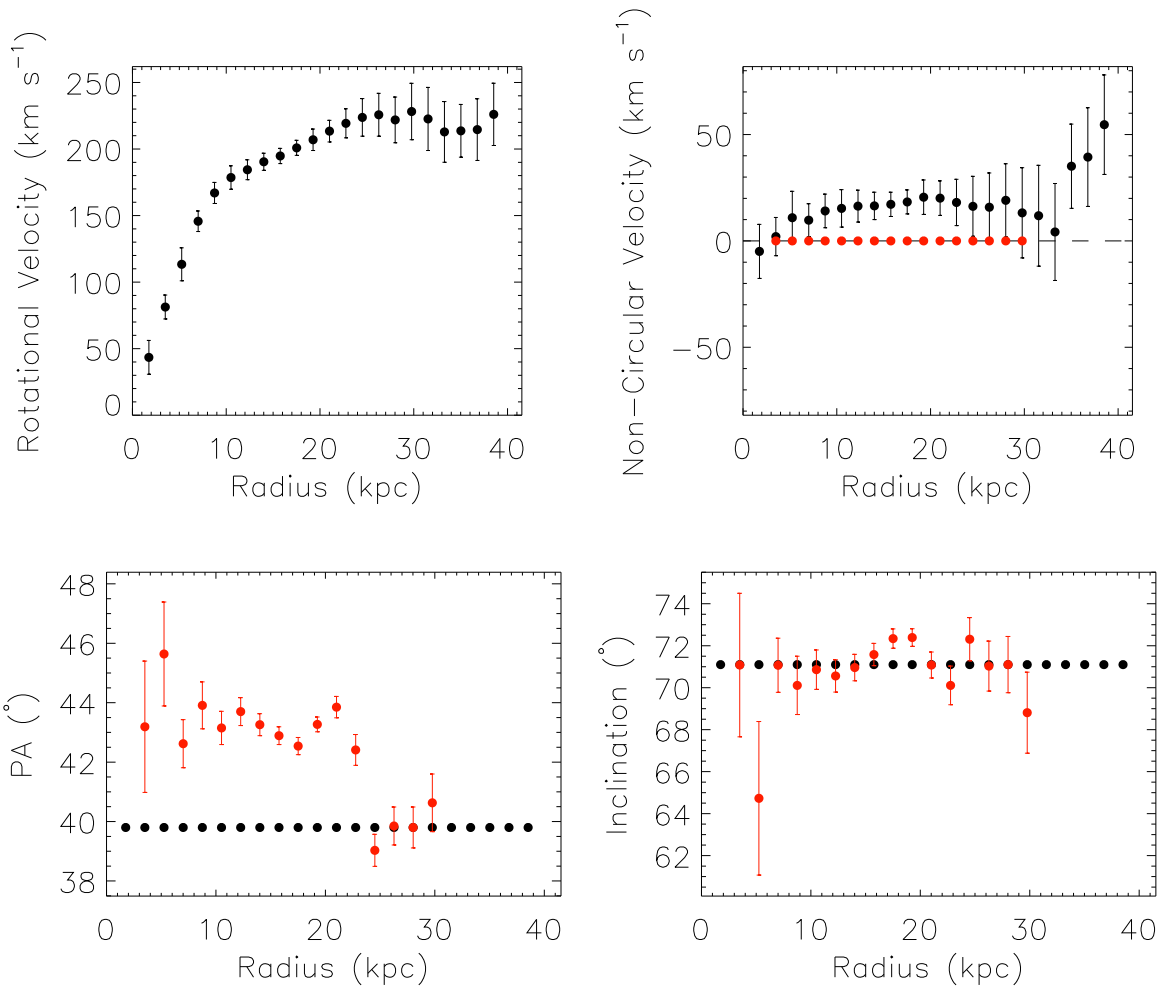


Figure 5. Rotation curve of UGC 7899 derived by fitting a tilted ring model (black circles). Panels are identical to Figure 2. The rotation curve quickly rises to a maximum speed of 200–250 km s⁻¹ at a radius of 10 kpc and remains flat. The noncircular velocities fit here prove to be only of marginal significance when reexamined with DiskFit. Instead, a model without noncircular velocities (red circles) is fit, which captures the warp with the abrupt change of the position angle at 25 kpc.

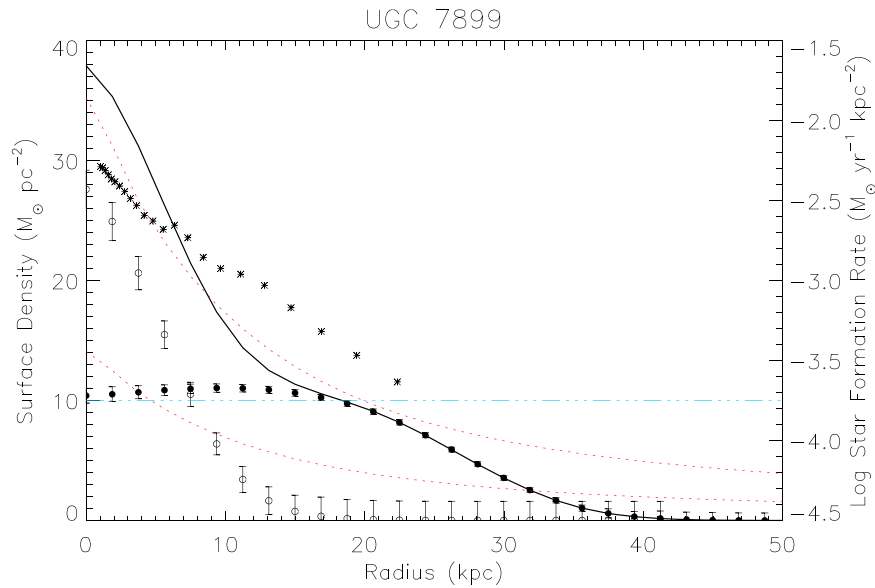


Figure 6. Surface density profile of the H I and H₂ in UGC 7899. Symbols are identical to Figure 3. Unlike UGC 6168 and NGC 5230, there is no hole in the H I. The H₂ surface densities reach 28 M_⊙ pc⁻², higher than either of the other two galaxies in this work by 50%. The gas appears marginally unstable according to Toomre Q at all radii inside of 30 kpc and becomes unstable in the inner 10 kpc, where the H₂ dominates the gas surface density.

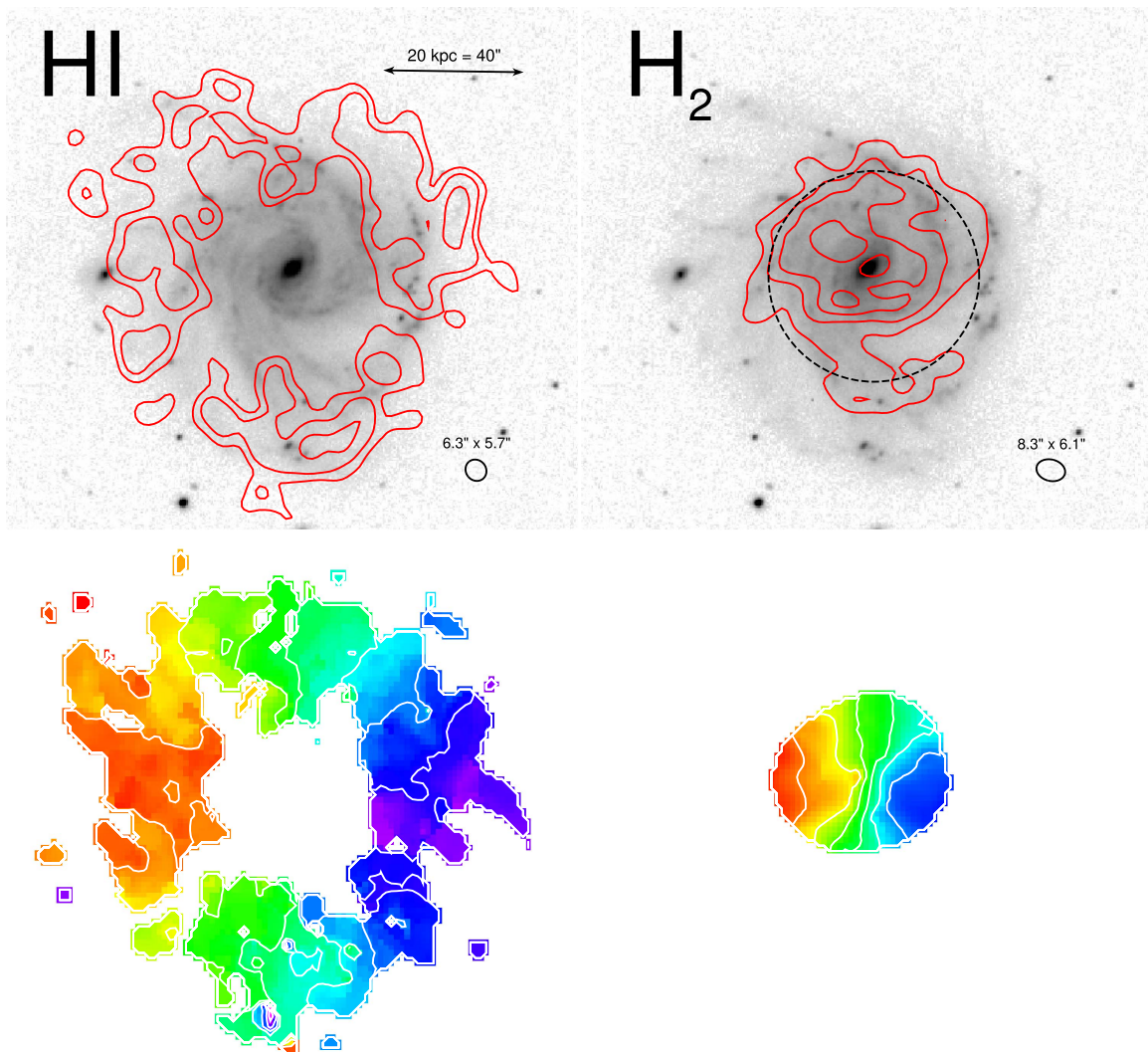


Figure 7. Integrated flux maps and velocity fields of NGC 5230. Panels are identical to Figure 1. The inclination of NGC 5230 is lower than for the other two galaxies ($i \sim 40^\circ$), allowing a clear view of the H I ring. CO emission reaches beyond the 50% response radius of CARMA ($\sim 30''$; dashed line), but not beyond the 20% response radius. The CO emission is resolved enough by CARMA to produce a rotation curve.

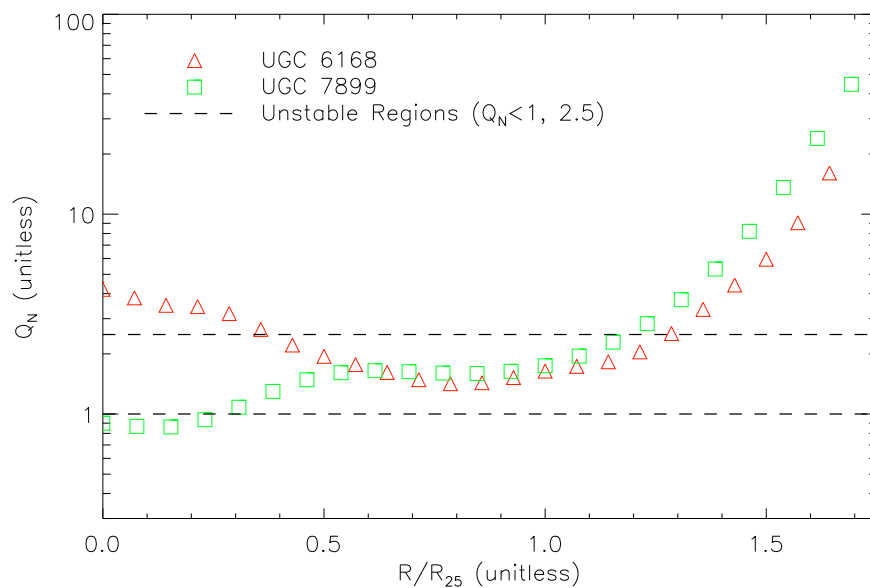


Figure 8. Multiphase Q_N from Romeo & Falstad (2013) for the three HighMass galaxies in this paper as a function of galactic radius. Radii are normalized to r -band R_{25} . Red open triangles are UGC 6168, and green open squares are UGC 7899. The black dashed line separates the unstable ($Q_N < 1$) and marginally stable ($Q_N \lesssim 2.5$) from the stable ($Q_N > 2.5$) regions.

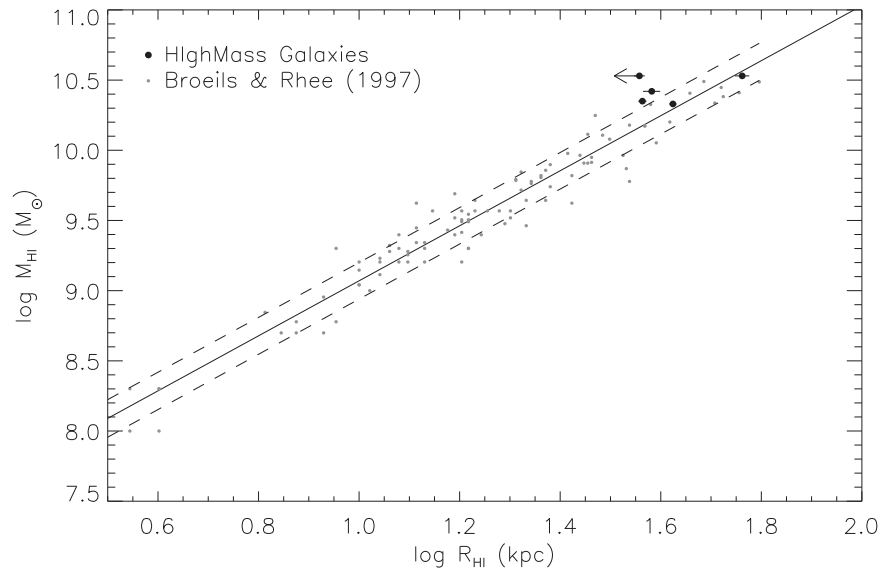


Figure 9. H I mass as a function of radius for the spiral and irregular galaxies of Broeils & Rhee (1997) (small gray filled circles), along with the best-fit line; the dashed line is the 1σ of the line. The larger black filled circles are HighMass galaxies. The three HighMass galaxies presented in this paper along with UGC 9037 lie to the left of the best-fit line (i.e., they have smaller R_{HI} than predicted), while only the LSB galaxy UGC 12506 is within the error of the line. For some of the HighMass galaxies, the uncertainties are smaller than the plotted points.

Equation (13) in Broeils & Rhee (1997)

$$\log \frac{\hat{R}_{\text{HI}}}{\text{kpc}} = 0.51 \log \frac{M_{\text{HI}}}{M_{\odot}} - 3.63. \quad (5)$$

Figure 9 presents this line, along with the Broeils & Rhee (1997) sample (gray filled circles). The HighMass galaxies are plotted in black. This relationship also holds true for the galaxies discussed by Hallenbeck et al. (2014)—UGC 9037 and UGC 12506. The H I disks of UGC 6168, UGC 7899, and NGC 5230 lie to the left of the line and so are more compact than expected. For NGC 5230, we have plotted assuming that $i = 0^\circ$, which yields the largest value of R_{HI} . For the three galaxies this difference is near the edge of significance (1.5σ – 2.9σ), but taken together, the difference is reasonably significant (3.6σ). Theoretically, the baryonic disk scale radius should increase with λ and the rotational velocity of the disk (e.g., Mo et al. 1998; Hernandez et al. 2007; Berta et al. 2008). This could indicate that these galaxies have somehow had their H I compressed, or that instabilities in the disk are allowing the normally extended, low-surface-density gas to flow inward. Table 2 presents the H I radii of all five galaxies, along with their expected H I radii.

3.6. Star Formation Efficiencies

It has already been observed that the HighMass galaxies have moderate to high values of $\text{SFE}(\text{H I}) \equiv \text{SFR}/M_{\text{HI}}$ relative to the ALFALFA sample as a whole (Huang et al. 2012b). In addition, our CARMA observations show that their SFRs are also typical for their H_2 masses: the H_2 depletion timescales ($\tau_{\text{H}_2} \equiv M_{\text{H}_2+\text{He}}/\text{SFR}$) are 0.3, 0.4, and 1.6×10^9 yr for UGC 6168, UGC 7899, and NGC 5230, respectively. These values are below the timescale observed by the THINGS survey of $(1.3$ – $3.6) \times 10^9$ yr (Leroy et al. 2008), as well as the 2.35×10^9 yr found by Bigiel et al. (2011). However, they overlap the predicted range found by the COLD GASS

Table 2
Observed and Expected H I Radii

Galaxy	R_{HI} (kpc)	\hat{R}_{HI} (kpc)
(1)	(2)	(3)
UGC 6168	36.6 (± 0.7)	45.0 (± 5.2)
UGC 7899	38.2 (± 1.5)	48.9 (± 5.7)
NGC 5230	36.1 (± 0.9) ^a	55.6 (± 6.6)
UGC 9037	42.1 (± 0.7)	43.9 (± 3.5)
UGC 12506	57.8 (± 1.9)	55.6 (± 4.5)

Note. Observed and expected H I radii of the three galaxies in this work and in Hallenbeck et al. (2014). Column (1): galaxy identifier. Column (2): observed radius where the H I reaches a deprojected surface density of $1 M_{\odot} \text{pc}^{-2}$, based on fitting the surface density profiles. Column (3): predicted H I radius, based on Equation (5) and Broeils & Rhee (1997).

^a This is an upper limit assuming that the inclination of NGC 5230 is face-on ($i = 0^\circ$).

survey for galaxies of similar stellar masses (Saintonge et al. 2011a, 2011b; $(0.8$ – $1.25) \times 10^9$ yr).

However, the globally averaged SFEs of H I and H_2 are just part of the story: the resolved SFE of our sample is likely to shed more light. The THINGS survey found several ways to parameterize the efficiency of the total gas (H I, H_2 , and He) as a function of galactic radius, normalized by R_{25} (see Equation (21) of Leroy et al. 2008). If we just consider the spiral galaxies in THINGS,

$$\text{SFE}(\text{gas}) = \begin{cases} 5.9 \times 10^{-10} & R < 0.4 R_{25} \\ 3.0 \times 10^{-10} \exp\left(-\frac{R}{0.25 R_{25}}\right) & R > 0.4 R_{25} \end{cases} \text{ yr}^{-1} \quad (6)$$

This form represents a constant value of SFE (H_2) and thus a constant SFE(gas) in the region of the interstellar medium (ISM) that is H_2 dominated ($\Sigma_{\text{H}_2} > \Sigma_{\text{HI}}$; $R \lesssim 0.4 R_{25}$). Outside of this region, the disk is H I dominated and the conversion of

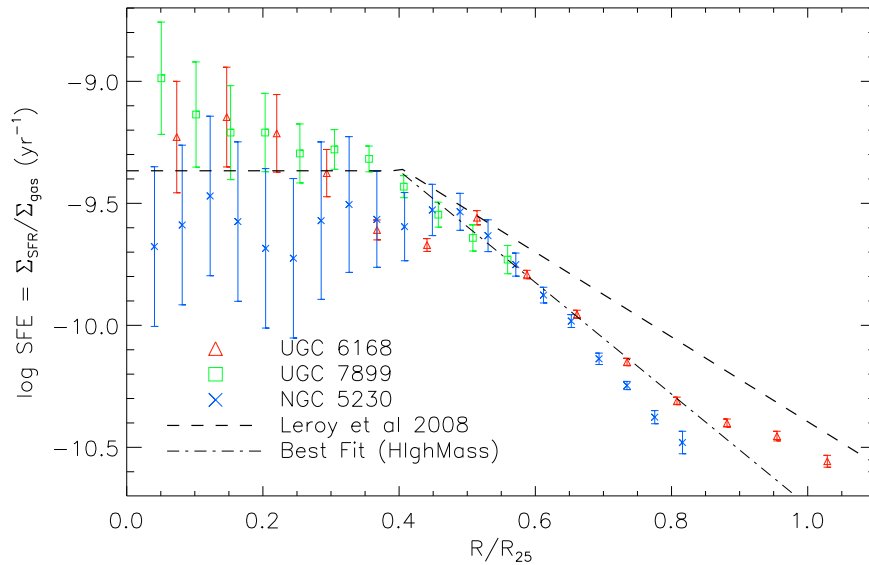


Figure 10. Total gas (H I, H₂, and He) SFE as a function of normalized galactic radius. Red open triangles are UGC 6168, green open squares are UGC 7899, and blue crosses are NGC 5230. The black dashed line represents a best-fit model for massive spirals found by THINGS (Leroy et al. 2008). The kink is near the transition from an H I-dominated to an H₂-dominated ISM; in the H I-dominated region, the SFE falls off exponentially with a scale length of $0.25 R_{25}$. In the H₂-dominated central regions of each galaxy, the HighMass galaxies follow the same trend as the massive THINGS spirals, but in the H I-dominated outskirts, the HighMass galaxies are all significantly less efficient at forming stars. The narrower dot-dashed line is a best fit to the HighMass galaxies alone, which have a shorter exponential scale length of $0.190(\pm 0.001) R_{25}$.

gas to stars becomes inefficient, declining exponentially with radius.

Figure 10 presents this fit, along with SFE(gas) for the three HighMass galaxies in this work. Red triangles, green squares, and blue crosses represent data for UGC 6168, UGCC 7899, and NGC 5230, respectively. Here, we include NGC 5230 because SFE(gas) depends on the ratio of two surface densities and so is independent of the assumed inclination. The dashed line is the parameterization in Equation (6). The HighMass galaxies in this work all exhibit the same overall trend of the THINGS parameterization: there is a core with nearly constant SFE(gas), and then at some radius, SFE begins to drop. At small radii, where the H₂ dominates the ISM, we see essentially no difference between the galaxies in our sample and the average spiral galaxy in the THINGS survey. In the outer disk, where the H I dominates the ISM, the SFE of our sample is significantly lower than for THINGS. The dot-dashed line is a best fit to the HighMass data, assuming an exponential decrease in SFE(gas) beyond $R > 0.4 R_{25}$. This has a significantly shorter scale length of $0.190(\pm 0.001) R_{25}$.

Given that the global SFE(H I) for these galaxies is typical, it is somewhat surprising to find that the resolved SFE(gas) is low where the ISM is primarily H I. This may be a consequence of the gas being unusually compact in these galaxies. The H α emission has been traced to only approximately $R/R_{25} < 1.0$. Of the total H I mass, 30% resides beyond this radius for UGC 6168 but only 3% for NGC 5230. For UGC 7899, this explanation is less conclusive: the star formation is only traced to $R/R_{25} < 0.6$, with 70% of the total H I mass residing beyond that radius.

A related possibility is that the relatively lower mass spiral sample of THINGS is a poor comparison sample. R_{25} for the THINGS galaxies varies between 10 and 20 kpc, while the three galaxies in this work have radii of 24–36 kpc (the HighMass sample as a whole has an average R_{25} of 20 kpc). The THINGS-derived SFE(gas) relationship has a factor of 2–3 scatter, and in general the galaxies with larger R_{25} in the

THINGS sample tend to fall below the relationship (Leroy et al. 2008). This may hint at a possible decrease in SFE scale radius at large galactic radii.

3.7. Dark Matter Properties

We model each galaxy with four components: an H I disk, an H₂ disk, a stellar disk, and dark matter. We use the H I and H₂ surface densities derived in Sections 2 and 2.1 and treat each as a thin disk. The stellar component is also modeled as a thin disk, using the stellar masses described in Section 2.2. The contribution of the dark matter can be determined via

$$V_{\text{obs}}^2 = V_{\text{H I}}^2 + V_{\text{H}_2}^2 + V_{\text{*}}^2 + V_{\text{DM}}^2 \quad (7)$$

where V_{obs} is the rotation curve, and the other velocities are the contributions from each phase. Both a Navarro–Frenk–White (NFW) and a pseudo-isothermal profile (ISO) are separately fit to the remaining V_{DM} component.

Using the methods of Querejeta et al. (2014) predicts mass-to-light ratios ($\Upsilon_{3,6}$) that are too high: the resulting stellar mass surface densities yield $V_{\text{*}}^2 > V_{\text{obs}}^2$ or unphysical parameters for dark matter fits ($c < 0$, for example). The $\Upsilon_{3,6}$ distribution has a spread of roughly 0.1 dex, which is insufficient to explain the difference. Instead, this is likely because we have not accounted for the effect of dust or stars of intermediate age contaminating the *Spitzer* 3.6 μm and 4.5 μm bands, which together can account for 20%–60% of the total infrared emission (Meidt et al. 2012). If we allow $\Upsilon_{3,6}$ to vary from its nominal value, best fits for both galaxies yield similarly inappropriate $\Upsilon_{3,6} \approx 0$. Instead, we set the average value of $\Upsilon_{3,6}$ such that the *Spitzer*-derived mass equals the mass from SED fitting. In such cases, we get good fits for both UGC 6168 and UGC 7899. This requires values of $\Upsilon_{3,6}$ a factor of 2–3 lower than the nominal values derived by Querejeta et al. (2014).

In Figure 11, we present both the dark matter fits to each galaxy’s rotation curve, using the NFW (left) and pseudo-isothermal (right) halo profiles. Black filled circles with

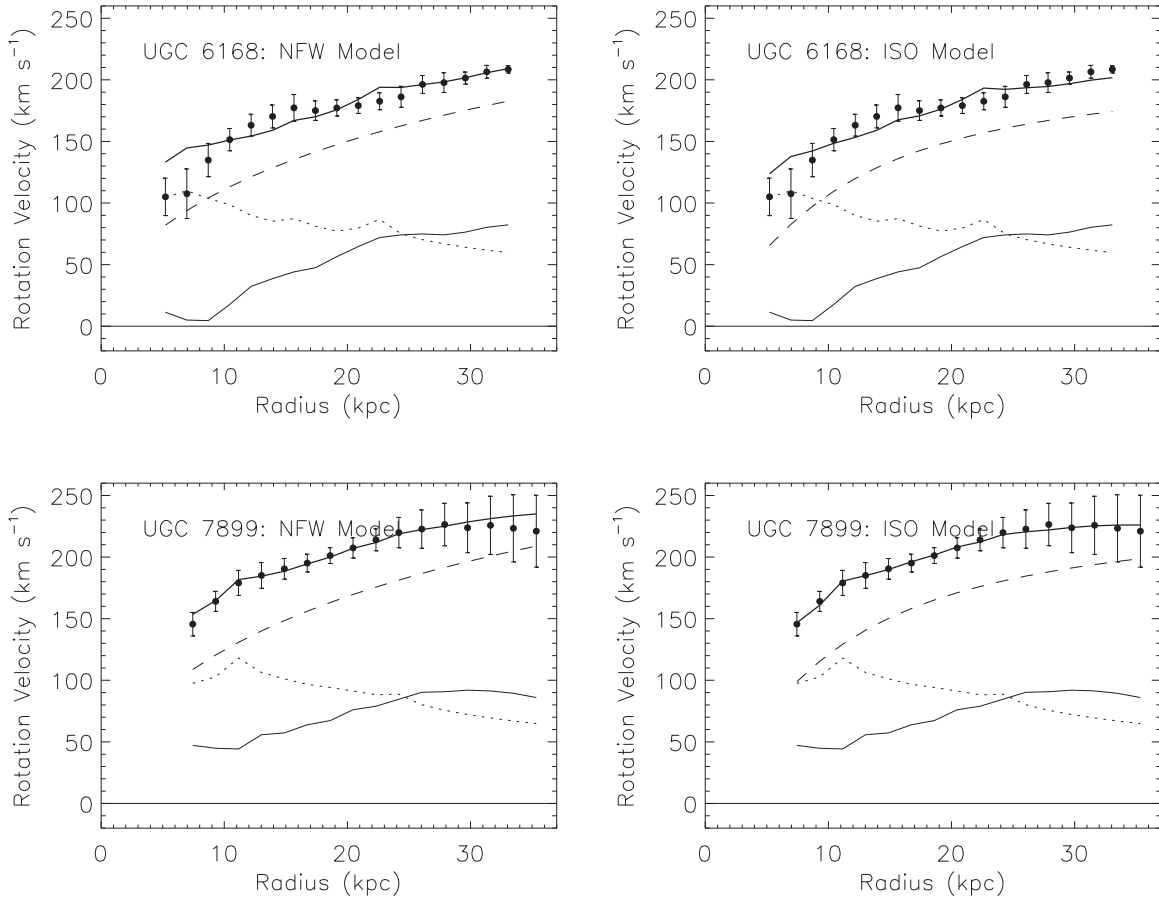


Figure 11. Rotation curves (black filled circles) and best-fit mass models (thick black lines) for UGC 6168 and UGC 7899. Long-dashed lines are dark matter halo fits using an NFW (left) or a pseudo-isothermal (right) profile. The thin black line is the total gas (H I, H₂, and He) contribution to the rotation curve, while the short-dashed line is the contribution from the stellar disk, after fitting $\Upsilon_{3.6}$. The dark matter is the dominant contributor to the rotation curve for every model. Fits for UGC 6168 and UGC 7899 are excellent for both halo profiles ($\chi^2_\nu \sim 0.5$).

Table 3
Dark Matter Fits

Galaxy	$\langle \Upsilon_{3.6} \rangle$ (M_\odot/L_\odot)	$\langle \Upsilon_{3.6}^{\text{SED}} \rangle$ (M_\odot/L_\odot)	c	NFW Fit R_{200} (kpc)	χ^2_ν	ρ_C ($10^{-3} M_\odot \text{pc}^{-2}$)	ISO Fit R_C (kpc)	χ^2_ν	Halo Spin λ
(1)	(2)	(3)	(4)	(5)	(6)	(7)	(8)	(9)	(10)
UGC 6168	0.45	0.27	1.47 ± 0.51	203 ± 36	1.03	9.2 ± 1.6	10.4 ± 1.3	0.41	0.09
UGC 7899	0.43	0.16	1.75 ± 0.29	224 ± 23	0.10	13.60 ± 0.52	9.00 ± 0.28	0.02	0.08

Note. Best-fit results of dark matter halo models to UGC 6168 and UGC 7899, using either a Navarro–Frenk–White (NFW) or pseudo-isothermal (ISO) dark matter halo model. Column (1): galaxy identifier. Column (2): nominal average mass-to-light ratio of each galaxy in the 3.6 μm band. Column (3): adopted mass-to-light ratio from setting total stellar mass from *Spitzer* observations equal to that calculated via SED fitting. Columns (4) and (5): concentration index and characteristic halo length scale. Column (6): reduced χ^2 of NFW fit. Columns (7) and (8): halo core density and length scale. Column (9): reduced χ^2 of ISO fit. Column (10): modified halo spin parameter, based on ISO fit.

uncertainties are the observed rotation curve. The thin solid black line is the total gas (H I+H₂+He) contribution, the short-dashed line is the stellar mass contribution, and the long-dashed line is the halo fit. The thick solid line is the summed contribution from each of the mass terms. For each galaxy, the dark matter is the dominant contributor to the rotation curve in the best-fit model at all radii. For UGC 6168 and UGC 7899, both the ISO and NFW profiles fit well ($\chi^2_\nu \sim 1$). Numerical results of the dark matter fits can be found in Table 3.

Figure 12 plots a histogram of dark matter halo spin parameters of three different samples. The solid histogram is the THINGS sample calculated as described in Hallenbeck

et al. (2014) and is normalized to unit area. For comparison is the volume-limited sample from the SDSS taken by Hernandez et al. (2007) and calculated from the global optical properties alone. The two distributions (and thus calculation methods) are roughly the same, especially accounting for the differences in sample size (19 THINGS galaxies versus 11,597 SDSS-selected galaxies). The remaining filled dotted bars are non-normalized counts of the galaxies from this work combined with Hallenbeck et al. (2014). UGC 12506 clearly has a high spin ($\lambda = 0.15$). UGC 6168, UGC 7899, and UGC 9037 all have values that are somewhat high, but not far into the tail ($\lambda \approx 0.09$).

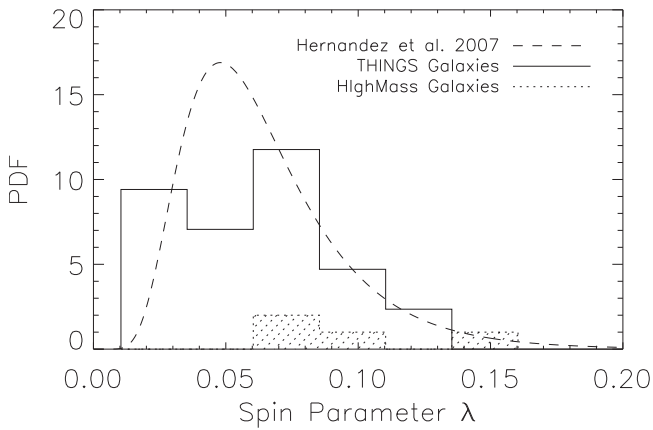


Figure 12. Dark matter halo spin parameters of three samples. The solid histogram is the THINGS sample, calculated from both local optical and gas properties according to the method of Hallenbeck et al. (2014), with area normalized. The dashed line is the best-fit probability density function calculated by Hernandez et al. (2007). That work uses global optical properties alone. The filled dotted histogram is from the sample in this work combined with Hallenbeck et al. (2014). There are two clear subsamples of HighMass galaxies: UGC 12506 has a high spin parameter (0.15), while UGC 9037, UGC 6168, and UGC 7899 have intermediate values.

4. DISCUSSION

UGC 9037 and UGC 12506—the two HighMass galaxies previously studied in detail by Hallenbeck et al. (2014)—were found to have very different properties. UGC 12506 has low surface densities of H I (typically $1\text{--}5 M_{\odot}\text{pc}^{-2}$ at radii from 10–40 kpc) and is an LSB galaxy. These properties can all be explained by its very high dark matter halo spin parameter ($\lambda = 0.15$). UGC 9037, on the other hand, has an above average but unexceptional spin parameter ($\lambda = 0.07$). Its H I has high ($>10 M_{\odot}\text{pc}^{-2}$) surface densities at $r < 10$ kpc, and correspondingly the Toomre Q at most radii was moderately unstable, especially in comparison with the stable H I disk of UGC 12506. UGC 9037 also has high-velocity gas inflows at all radii. UGC 9037’s above average spin parameter may have suppressed star formation over much of cosmic history. However, the high surface densities of H I and inflowing gas suggest a recent enhancement in star formation in comparison with its time-averaged rate. We thus see two very different states for these two galaxies: UGC 12506 remains in a low-surface-density, suppressed star formation state, while UGC 9037 is beginning a phase of enhanced star formation—possibly triggered by recently acquired gas.

Overall, the three galaxies discussed in this work (UGC 6168, UGC 7899, and NGC 5230) appear more like UGC 9037 than UGC 12506. First, none of the three are LSB galaxies. They all have typical SFRs for their H_2 masses and have short SFE scale lengths—that is, their star formation quickly becomes extremely inefficient where the ISM is H I dominated in comparison with the THINGS sample. These properties strongly suggest that any possible star formation bottleneck is in the H I-to- H_2 conversion, and not in the conversion of H_2 to H I. In addition, for the two galaxies for which a spin parameter can be measured (UGC 6168 and UGC 7899), λ is found to be above average, but not exceptionally so, and gas surface densities are found to reach typical values ($\sim 10 M_{\odot}\text{pc}^{-2}$) over a range of radii. This is in contrast with the theoretical prediction that higher spin parameters are theoretically associated with lower gas and star formation surface densities

(e.g., Boissier & Prantzos 2000). We thus claim that the galaxies in this work are transitioning from a long history of suppressed star formation to a more active phase. These findings are in agreement with Huang et al. (2014), who came to the same conclusion based on studying the $H\alpha$ emission of the HighMass galaxies.

UGC 6168, like UGC 9037, is observed to have a moderately unstable gas disk across a wide range of radii. It is also possible that UGC 6168 has inflowing gas, but the observed noncircular flows in the galaxy are of only marginal ($1\sigma\text{--}2\sigma$) significance. The strongest indication of noncircular flows is the misalignment between the average position angle of the H I and CO gas phases. It does not have the high H I surface densities observed in UGC 9037, instead saturating at the typical $10 M_{\odot}\text{pc}^{-2}$. Finally, we have calculated its spin parameter to be $\lambda = 0.09$, an above average but not extremely large value.

UGC 7899 shares many properties with UGC 6168 and UGC 9037: it is not an LSB, it has a moderately unstable disk, and it has an above average λ . Like the previously studied UGC 9037, the H I in the center of the galaxy is not depleted, but saturates at $10 M_{\odot}\text{pc}^{-2}$; we also see high surface densities of H_2 . Unlike UGC 6168 and UGC 7899, there is no evidence of noncircular motion in the gas disk of the galaxy. It is unique among the HighMass galaxies so far presented in that its disk shows some warping, which could be indicative of recent cold accretion from the intergalactic medium. However, warps in H I disks at large radii have long been observed to be common, even in relatively isolated galaxies (Sancisi 1976; Bosma 1981; Briggs 1990; van der Kruit & Freeman 2011).

Because we are unable to make a clear case for the inclination—and thus the surface densities or dark matter profile—the case for NGC 5230 is more difficult. It is easiest to compare it with the other galaxies in this work: despite high H I gas masses and gas fractions, all three show typical values of SFE(H I) and SFE(gas) in comparison with other H I-selected galaxies and the optically selected GASS sample, respectively. All three show a shorter SFE length scale than for the local spirals of THINGS. In addition, all three show evidence for a much smaller $R_{H I}$ than is expected for their H I masses, regardless of what inclination is assumed for NGC 5230.

NGC 5230’s neighbors may be the most important clues to understanding the galaxy. There are two galaxies of similar size within 1 Mpc of NGC 5230: NGC 5222, at a projected distance of 300 kpc to the west, and NGC 5221, 400 kpc to the northwest. NGC 5222 is an elliptical galaxy hosting an active galactic nucleus and has an optically much smaller blue companion. More interesting is NGC 5221, an irregular spiral with a long tail pointing to the northwest. An optical image of NGC 5230 and its neighbors can be found in Figure 13, with contours from ALFALFA overlaid. These three galaxies are embedded in a common H I envelope with a significant amount of gas: both NGC 5222’s blue companion and NGC 5221 are detected in ALFALFA, with $\log M_{H I} = 9.96$ and 10.02, respectively. A number of tidal tails and otherwise extragalactic gas can be observed in the ALFALFA data cubes. A bridge between NGC 5230 and NGC 5221 is visible, and tails between NGC 5222 and its neighbors are possible but unresolved due to the large (~ 120 kpc at 88 Mpc) ALFALFA beam. It is thus a strong possibility that NGC 5230’s current state is due to its clear interaction with its neighbors. Its gas is likely compressed due to tidal torques, yet its SFE can remain low because much

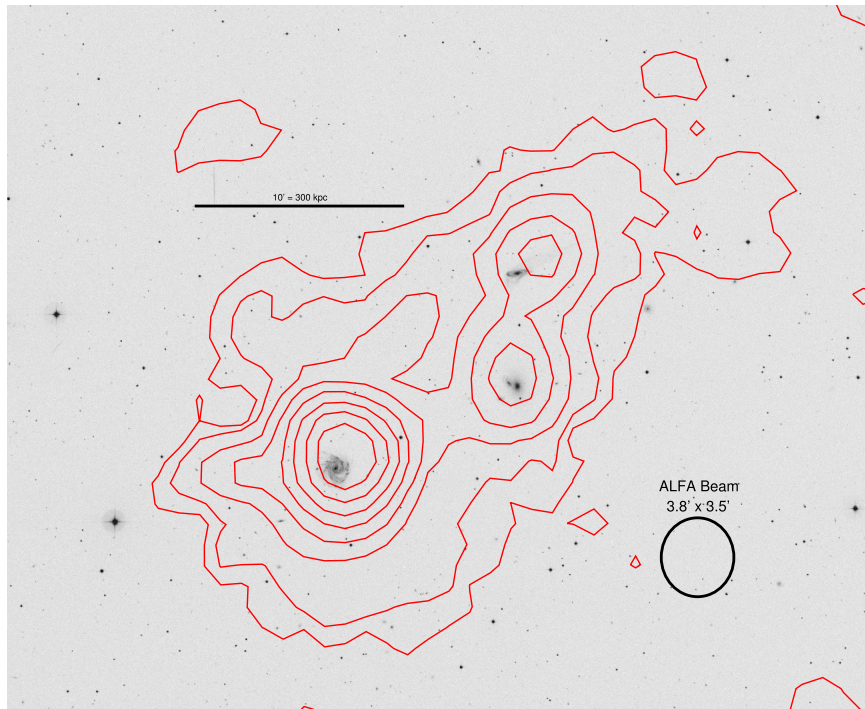


Figure 13. Optical (DSS II/Blue) image of NGC 5230 (east) and its neighbors NGC 5222 (elliptical galaxy; west) and NGC 5221 (irregular spiral; northwest). Overlaid are ALFALFA contours, starting from $0.1 \text{ Jy km s}^{-1} \text{ beam}^{-1}$ (3σ) and increasing by a factor of $\sqrt{2}$ at each additional contour. The peaks are roughly 10 and $3 \text{ Jy km s}^{-1} \text{ beam}^{-1}$ for NGC 5230 and each of its neighbors, respectively. Several tidal tails and bridges are clearly visible outside the optical galaxies, as well as a significant amount of low column density gas distributed throughout the group. The apparent tail from NGC 5230 pointing to the east is most likely an artifact from the ALFA beam and the ALFALFA grids, and not a real feature.

of the gas nominally associated with it is extended and at low column density.

5. CONCLUSIONS

The HighMass sample is a selection of 34 galaxies from the ALFALFA 40% data release that all have high H I masses and are all gas-rich for their stellar masses. We have presented resolved H I and H₂ studies of three HighMass galaxies, UGC 6168, UGC 7899, and NGC 5230. Along with UGC 9037 and UGC 12506, this brings the total number of resolved gas studies of the HighMass galaxies to five. None of the galaxies in this work appear to host extremely high dark matter spin parameters like UGC 12506. Instead, most of the galaxies so far appear more like the previously studied UGC 9037: galaxies in transition from a gas-rich but inactive phase to a phase of active star formation. The galaxies in this work display the following properties:

1. *High HI masses and high gas fractions* compared with an optically selected sample, like all HighMass galaxies.
2. *More concentrated HI disks* are observed than are expected for their H I masses. This was not observed in either of the HighMass galaxies previously studied.
3. *Moderately unstable disks*, with values of both Toomre Q and the Q_N of Romeo & Falstad (2013) $\lesssim 2$ over a wide range of radii, are observed in UGC 6168 and UGC 7899.
4. *Typical H₂ SFEs* compared with two optically selected samples: the local spiral galaxies of THINGS and COLD GASS galaxies of similar stellar mass. This comparison holds for both global (both samples) and resolved SFEs (THINGS).

5. *Mixed HI SFEs.* Globally, their SFE(H I) is typical for an H I-selected sample, but in the H I-dominated region of each galaxy, SFE as a function of radius declines with a shorter scale length ($0.19 R_{25}$) than the spirals of the THINGS sample ($0.25 R_{25}$).
6. *Above average spin parameters* compared with an optically selected sample are observed for UGC 6168 and UGC 7899 ($\lambda = 0.09$ and 0.08); we cannot directly measure λ for NGC 5230.

Individually, there are a few unique features in each galaxy, which hint at their past and why their H I content is so large for their stellar masses:

1. *For UGC 6168*, the average position angles in the H I and H₂ phases do not match, which indicates noncircular motions in its gas disk.
2. *UGC 7899* is the only HighMass galaxy thus far for which a warp has been observed in the outer H I disk, which may be indicative of accretion of cold gas from the intergalactic medium.
3. *NGC 5230* has two lower-mass neighbors, all sharing a common H I envelope. Its high H I mass but typical SFR may be partially explained by gas taken from its neighbors that has not yet settled into the galactic disk.

This work has been supported by NSF-AST-0606007 and AST-1107390, NASA/JPL Spitzer RSA/73350, grants from the Brinson Foundation, and a Student Observing Support award from NRAO.

This work is based in part on observations made with the Combined Array for Research in Millimeter-wavelength Astronomy (CARMA). Support for CARMA construction

was derived from the Gordon and Betty Moore Foundation, the Kenneth T. and Eileen L. Norris Foundation, the James S. McDonnell Foundation, the Associates of the California Institute of Technology, the University of Chicago, the states of California, Illinois, and Maryland, and the National Science Foundation. CARMA development and operations were supported by the National Science Foundation under a cooperative agreement and by the CARMA partner universities.

This work is based in part on observations made with the Karl G. Jansky Very Large Array, a facility of the National Radio Astronomy Observatory (NRAO). The NRAO is a facility of the National Science Foundation operated under cooperative agreement by Associated Universities, Inc.

This work is based in part on observations made with the Arecibo Observatory. The Arecibo Observatory is operated by SRI International under a cooperative agreement with the National Science Foundation (AST-1100968), and in alliance with Ana G. Méndez-Universidad Metropolitana and the Universities Space Research Association. This work is based in part on observations made with the *Spitzer Space Telescope*, which is operated by the Jet Propulsion Laboratory, California Institute of Technology, under a contract with NASA.

This work has made use of THINGS, “The H I Nearby Galaxy Survey” (Walter et al. 2008).

REFERENCES

- Abdo, A. A., Ackermann, M., Ajello, M., et al. 2010, *ApJ*, **710**, 133
 Arimoto, N., Sofue, Y., & Tsujimoto, T. 1996, *PASJ*, **48**, 275
 Begeman, K. G. 1989, *A&A*, **223**, 47
 Bell, E. F., McIntosh, D. H., Katz, N., & Weinberg, M. D. 2003, *ApJS*, **149**, 289
 Berta, Z. K., Jimenez, R., Heavens, A. F., & Panter, B. 2008, *MNRAS*, **391**, 197
 Bigiel, F., Leroy, A., Walter, F., et al. 2008, *AJ*, **136**, 2846
 Bigiel, F., Leroy, A. K., Walter, F., et al. 2011, *ApJL*, **730**, L13
 Blitz, L., Fukui, Y., Kawamura, A., et al. 2007, in *Protostars and Planets V*, Giant Molecular Clouds in Local Group Galaxies, ed. D. Reipurth, D. Jewitt, & K. Keil (Tucson, AZ: Univ. Arizona Press), 81
 Boissier, S., & Prantzos, N. 2000, *MNRAS*, **312**, 398
 Bolatto, A. D., Wolfire, M., & Leroy, A. K. 2013, *ARA&A*, **51**, 207
 Bosma, A. 1981, *AJ*, **86**, 1791
 Bothun, G. D., Impey, C. D., Malin, D. F., & Mould, J. R. 1987, *AJ*, **94**, 23
 Briggs, F. H. 1990, *ApJ*, **352**, 15
 Brinchmann, J., Charlot, S., White, S. D. M., et al. 2004, *MNRAS*, **351**, 1151
 Broeils, A. H., & Rhee, M.-H. 1997, *A&A*, **324**, 877
 Catinella, B., & Cortese, L. 2015, *MNRAS*, **446**, 3526
 Catinella, B., Schiminovich, D., Kauffmann, G., et al. 2010, *MNRAS*, **403**, 683
 Cervantes-Sodi, B., & Hernández, X. 2009, *RMxAA*, **45**, 75
 Dame, T. M., Hartmann, D., & Thaddeus, P. 2001, *ApJ*, **547**, 792
 Draine, B. T., Dale, D. A., Bendo, G., et al. 2007, *ApJ*, **663**, 866
 Fazio, G. G., Hora, J. L., Allen, L. E., et al. 2004, *ApJS*, **154**, 10
 Fraternali, F., & Binney, J. J. 2006, *MNRAS*, **366**, 449
 Fraternali, F., & Binney, J. J. 2008, *MNRAS*, **386**, 935
 Fraternali, F., Oosterloo, T., Sancisi, R., & van Moorsel, G. 2001, *ApJL*, **562**, L47
 Hallenbeck, G., Huang, S., Spekkens, K., et al. 2014, *AJ*, **148**, 69
 Haynes, M. P., Giovanelli, R., Martin, A. M., et al. 2011, *AJ*, **142**, 170
 Hernandez, X., Park, C., Cervantes-Sodi, B., & Choi, Y.-Y. 2007, *MNRAS*, **375**, 163
 Heyer, M., Krawczyk, C., Duval, J., & Jackson, J. M. 2009, *ApJ*, **699**, 1092
 Huang, S., Haynes, M. P., Giovanelli, R., et al. 2012a, *AJ*, **143**, 133
 Huang, S., Haynes, M. P., Giovanelli, R., et al. 2014, *ApJ*, **793**, 40
 Huang, S., Haynes, M. P., Giovanelli, R., & Brinchmann, J. 2012b, *ApJ*, **756**, 113
 Jimenez, R., Padoan, P., Matteucci, F., & Heavens, A. F. 1998, *MNRAS*, **299**, 123
 Kennicutt, R. C., Jr. 1989, *ApJ*, **344**, 685
 Kuzio de Naray, R., Arsenault, C. A., Spekkens, K., et al. 2012, *MNRAS*, **427**, 2523
 Lee, C., Chung, A., Yun, M. S., et al. 2014, *MNRAS*, **441**, 1363
 Lelli, F., Fraternali, F., & Sancisi, R. 2010, *A&A*, **516**, A11
 Lemonias, J. J., Schiminovich, D., Catinella, B., Heckman, T. M., & Moran, S. M. 2014, *ApJ*, **790**, 27
 Leroy, A. K., Walter, F., Brinks, E., et al. 2008, *AJ*, **136**, 2782
 Macciò, A. V., Dutton, A. A., van den Bosch, F. C., et al. 2007, *MNRAS*, **378**, 55
 Marinacci, F., Binney, J., Fraternali, F., et al. 2010, *MNRAS*, **404**, 1464
 Martin, C. L., & Kennicutt, R. C., Jr. 2001, *ApJ*, **555**, 301
 Meidt, S. E., Schinnerer, E., Knapen, J. H., et al. 2012, *ApJ*, **744**, 17
 Mo, H. J., Mao, S., & White, S. D. M. 1998, *MNRAS*, **295**, 319
 Oppenheimer, B. D., Davé, R., Kereš, D., et al. 2010, *MNRAS*, **406**, 2325
 Papastergis, E., Cattaneo, A., Huang, S., Giovanelli, R., & Haynes, M. P. 2012, *ApJ*, **759**, 138
 Querejeta, M., Meidt, S. E., Schinnerer, E., et al. 2014, arXiv:1410.0009
 Rafikov, R. R. 2001, *MNRAS*, **323**, 445
 Romeo, A. B., & Falstad, N. 2013, *MNRAS*, **433**, 1389
 Romeo, A. B., & Wiegert, J. 2011, *MNRAS*, **416**, 1191
 Saintonge, A., Kauffmann, G., Kramer, C., et al. 2011a, *MNRAS*, **415**, 32
 Saintonge, A., Kauffmann, G., Wang, J., et al. 2011b, *MNRAS*, **415**, 61
 Salim, S., Rich, R. M., Charlot, S., et al. 2007, *ApJS*, **173**, 267
 Sancisi, R. 1976, *A&A*, **53**, 159
 Sandstrom, K. M., Leroy, A. K., Walter, F., et al. 2013, *ApJ*, **777**, 5
 Schiminovich, D., Catinella, B., Kauffmann, G., et al. 2010, *MNRAS*, **408**, 919
 Schiminovich, D., Wyder, T. K., Martin, D. C., et al. 2007, *ApJS*, **173**, 315
 Sellwood, J. A., & Sánchez, R. Z. 2010, *MNRAS*, **404**, 1733
 Solomon, P. M., Downes, D., Radford, S. J. E., & Barrett, J. W. 1997, *ApJ*, **478**, 144
 Spekkens, K., & Sellwood, J. A. 2007, *ApJ*, **664**, 204
 Strong, A. W., & Mattox, J. R. 1996, *A&A*, **308**, L21
 Toomre, A. 1964, *ApJ*, **139**, 1217
 van der Kruit, P. C., & Freeman, K. C. 2011, *ARA&A*, **49**, 301
 Walter, F., Brinks, E., de Blok, W. J. G., et al. 2008, *AJ*, **136**, 2563
 Wang, B., & Silk, J. 1994, *ApJ*, **427**, 759
 Wang, J., Kauffmann, G., Józsa, G. I. G., et al. 2013, arXiv:1303.3538
 Wang, J., Koribalski, B. S., Serra, P., et al. 2016, *MNRAS*, **460**, 2143
 Werner, M. W., Roellig, T. L., Low, F. J., et al. 2004, *ApJS*, **154**, 1
 Wilson, C. D. 1995, *ApJL*, **448**, L97
 Wilson, C. D., Warren, B. E., Irwin, J., et al. 2011, *MNRAS*, **410**, 1409